AGU ADVANCING EARTH AND SPACE SCIENCES

Water Resources Research

RESEARCH ARTICLE
10.1029/2023WR034770

# General Local Reactive Boundary Condition for Dissolution and Precipitation Using the Lattice Boltzmann Method

**J. Weinmiller[1,2], M. P. Lautenschlaeger[1,2], B. Kellers[1,2], T. Danner[1,2], and A. Latz[1,2,3]**

[1]German Aerospace Center (DLR), Institute of Engineering Thermodynamics, Ulm, Germany, [2]Helmholtz Institute Ulm for Electrochemical Energy Storage (HIU), Ulm, Germany, [3]Ulm University (UUlm), Institute of Electrochemistry, Ulm, Germany

**Key Points:**

- An extensively validated new general local reactive boundary condition (RBC) is presented
- A comprehensive comparison of this RBC with other existing general local RBC was performed
- Our RBC is combined with the rest fraction and applied to simulate dissolution and precipitation phenomena

**Supporting Information:**

Supporting Information may be found in the online version of this article.

**Correspondence to:**

J. Weinmiller,
julius.weinmiller@dlr.de

**Citation:**

Weinmiller, J., Lautenschlaeger, M. P., Kellers, B., Danner, T., & Latz, A. (2024). General local reactive boundary condition for dissolution and precipitation using the lattice Boltzmann method. *Water Resources Research*, *60*, e2023WR034770. https://doi.org/10.1029/2023WR034770

Received 20 JUN 2023
Accepted 26 JAN 2024

**Author Contributions:**

**Conceptualization:** T. Danner
**Data curation:** J. Weinmiller
**Formal analysis:** J. Weinmiller
**Funding acquisition:** T. Danner, A. Latz
**Investigation:** J. Weinmiller
**Methodology:** J. Weinmiller, M. P. Lautenschlaeger
**Project administration:** T. Danner
**Resources:** M. P. Lautenschlaeger, T. Danner, A. Latz
**Software:** J. Weinmiller
**Supervision:** T. Danner, A. Latz
**Validation:** J. Weinmiller, M. P. Lautenschlaeger, B. Kellers
**Visualization:** J. Weinmiller
**Writing – original draft:** J. Weinmiller
**Writing – review & editing:** M. P. Lautenschlaeger, B. Kellers



**Abstract** A general and local reactive boundary condition (RBC) for studying first-order equilibrium reactions using the lattice Boltzmann method is presented. Its main characteristics are accurate reproduction of wall diffusion, invariance to the wall and grid orientation, and absence of nonphysical artifacts. The scheme is successfully tested for different benchmark cases considering diffusion, advection, and reactions of fluids at solid-liquid interfaces. Unlike other comparable RBCs from the literature, the novel scheme is valid for a large range of Péclet and Damköhler numbers, and shows realistic pattern formation during precipitation. In addition, quantitative results are in good accordance with analytical solutions and values from literature. Combining the new RBC with the rest fraction method, Péclet-Reynolds ratios of up to 1,000 can be achieved. Overall, the novel RBC accurately models first-order reactions, is applicable for complex geometries, and allows efficiently simulating dissolution and precipitation phenomena in fluids at the pore scale.

## 1. Introduction

Dissolution and precipitation of solid solutes occur in a broad range of natural phenomena and technological applications. Typical examples are dissolution of minerals in subsurface hydrology (Andrews et al., 2023; Baqer & Chen, 2022; Přikryl et al., 2017), biofilm growth in nutrient rich environments (Jung & Meile, 2021), etching into substrates (Cui et al., 2019), and conversion of active material in energy storage systems (Danner & Latz, 2019; Fang et al., 2021).

Despite their omnipresence, a detailed experimental analysis of such processes is often lacking due to the dominant small length and short time scales on which they occur. As such, computational methods and more specifically continuum approaches are used to describe these phenomena on the macroscale. But even they are stretched to their limits, when dissolution and precipitation occur in structurally complex porous media where the relevant physics happen at the microscopic pore scale.

A computational method that has proven to give insight into such mesoscopic phenomena—between micro- and macroscales—is the lattice Boltzmann method (LBM). It can be applied to predict flow, transport, and reactions in porous media (Guiltinan et al., 2021; Lautenschlaeger et al., 2023; Liu et al., 2021). Especially over the last decade, LBM has gained importance both technically and application-wise. On the one hand, the ease of meshing and parallelization makes LBM extremely favorable for high-performance computing (Kellers et al., 2023; Krause et al., 2021; Latt et al., 2021). On the other hand, it can be applied to a broad variety of application fields. In the context of porous media these are for example,: oil and gas flow in underground formations (H. Li et al., 2015; Ren et al., 2015), oil recovery with in situ combustion (Lei & Luo, 2022), pore structure evolution in cement manufacturing (Patel et al., 2014, 2021), combustion of porous solid rocket fuel (Wang & Zhu, 2018), water transport and reactions in fuel cells (Sarkezi-Selsky et al., 2022), multi-phase flow in batteries (Danner et al., 2016; Lautenschlaeger, Prifling, et al., 2022; Lautenschlaeger, Weinmiller, et al., 2022), and dissolution and precipitation reactions in stone formations (Chen et al., 2014; Kang & Lichtner, 2013; Tian & Wang, 2017; L. Zhang et al., 2019).

In most of these cases, dissolution and precipitation play an important role. Using LBM, such reactions are typically modeled as heterogeneous reactive boundary conditions (RBC). Different approaches to translate macroscopic reaction behavior into mesoscopic schemes are known from literature. They range from simple modified bounce-back schemes (Kang et al., 2002, 2007), over pseudo-homogeneous reactions (Patel et al., 2014), and schemes based on interpolation using the wall normal (Chen et al., 2013; L. Li et al., 2017;

Walsh & Saar, 2010; Xie et al., 2021), up to general local boundary schemes for first-order (Ju et al., 2020; Patel, 2016; Verhaeghe et al., 2006) and higher-order reactions (Hiorth et al., 2013; Kashani et al., 2022). Two important scheme characteristics are *generality* and *locality*. Here, *general* means that the underlying scheme is the same regardless of the surrounding cells, that is, corners, edges and flat boundaries use the same scheme. Whereas *local* means that only information of the current boundary cell is used. In combination, they are a necessary basis for versatile and computationally efficient RBCs applicable to complex geometries.

Several approaches have been considered to derive such general local boundary schemes, of which three are discussed in more detail in this paper: (a) Verhaeghe et al. (2006) was amongst the first to develop such a model for multi-component LBM using the momentum transfer analysis of Bouzidi et al. (2001). (b) Patel (2016) developed an approach that bases on bouncing back the non-equilibrium part and including the flux as a concentration gradient while correctly capturing the macroscopic wall diffusion. (c) Ju et al. (2020) extended an approach, which was originally developed for finite differences (T. Zhang et al., 2012) and then converted to a local scheme (Meng & Guo, 2016), to also consider the correct macroscopic wall diffusion. All aforementioned RBC schemes show robust behavior in cases where the RBC normal is aligned with the lattice. However, cases different from these benchmarks are either missing in the corresponding papers or they show a nonphysical behavior of the corresponding scheme there.

Therefore, in this paper, a novel RBC scheme is presented which is based on the work of Verhaeghe et al. (2006), Ju et al. (2020), and Patel (2016). It is shown to overcome most deficiencies of these methods. It captures the correct wall diffusion and wall normal behavior, and is applicable to a broad range of reaction regimes. It is shown that the new RBC scheme can be combined with the rest fraction method (Sullivan, Johns, et al., 2005) to enable numerically stable simulations even at large ratios between the solute diffusivity and solvent viscosity.

The new RBC scheme as well as the RBC schemes of Verhaeghe et al. (2006), Ju et al. (2020), and Patel (2016) are tested using numerous benchmark cases that vary in complexity. For the sake of comparability, all schemes are reformulated to a common notation. The test cases include: (a) A robust reaction-diffusion verification case for which analytical solutions exists. (b) Pattern formation in a precipitation process. (c) A sophisticated benchmark case from the literature (Molins et al., 2020), considering reactions in channel flow. The latter setup is used to demonstrate the new RBC scheme's capability to handle complex media as well. All simulations are conducted in 2D. They can, however, be easily extended to 3D.

The paper is organized as follows: In Section 2, LBM basics, the rest fraction method, as well as the coupling of LBM to dissolution and precipitation are introduced. This section also covers the reformulation of the aforementioned RBC schemes. The verification and validation of the different schemes are compared and discussed in Section 3. Finally, the findings are summarized and conclusions are given in Section 4.

## 2. Numerical Methods

All LBM simulations presented in this work were conducted using an extended version of the LBM simulation package Palabos (Latt et al., 2021). There, the rest fraction method, reactive boundary conditions, and dissolution and precipitation were implemented.

### 2.1. LBM Fundamentals

For classical fluid flow, LBM solves the Boltzmann equation discretized in the phase-space mostly on a uniform grid. The velocity space is represented by the so-called lattice. It consists of a set of velocities $\{\mathbf{e}_i\}$, weights $\{w_i\}$ and a specific lattice speed of sound $c_s$. It forms the framework to distribute a set of particles that are represented by a particle distribution function, typically called population. In the following, it is indicated by either $f_i$ or $g_i$, where $i$ is the lattice direction. Fluid flow emerges through local collision and subsequent streaming of the populations. For reactive flows, the hydrodynamic carrier fluid and the advected scalar field are distinguished using separate lattices and equations. They are coupled by the fluid velocity, determined from the carrier fluid, which enters the advected scalar field.

#### 2.1.1. Hydrodynamic Equations

The dynamics of the carrier fluid described by the Navier-Stokes (NS) equations are solved using the lattice Boltzmann equation combined with the well-known BGK collision operator (Krüger et al., 2017)

$$f_i(\mathbf{x}+\mathbf{e}_i\Delta t, t+\Delta t) = f_i(\mathbf{x}, t) - \frac{1}{\tau_{\mathrm{NS}}}\left(f_i(\mathbf{x}, t) - f_i^{\mathrm{eq}}(\mathbf{x}, t)\right), \tag{1}$$

where $\tau_{\mathrm{NS}}$ is the relaxation time which is determined by the fluid viscosity $\nu = c_s^2(\tau_{\mathrm{NS}} - 0.5)$ and $f_i^{\mathrm{eq}}$ is the equilibrium population

$$f_i^{\mathrm{eq}}(\rho, \mathbf{u}) = \mathrm{w}_i\rho\left(1 + \frac{\mathbf{e}_i\cdot\mathbf{u}}{c_s^2} + \frac{(\mathbf{u}\cdot\mathbf{e}_i)^2}{2c_s^4} - \frac{\mathbf{u}\cdot\mathbf{u}}{2c_s^2}\right). \tag{2}$$

The fluid density $\rho$ and the fluid velocity $\mathbf{u}$ are determined from $f_i$ as

$$\rho = \sum_i f_i, \qquad \rho\mathbf{u} = \sum_i f_i\mathbf{e}_i. \tag{3}$$

In the following, the D2Q9 lattice is applied to solve the hydrodynamic equations in 2D. Further details are given in Appendix A.

At high relaxation times, the BGK collision operator introduces numerical slip at bounce-back walls leading to inaccuracies and instabilities. To overcome these artifacts, the two relaxation time (TRT) collision operator (Ginzburg et al., 2008; d'Humières & Ginzburg, 2009) is used in such cases. It is given as

$$\begin{aligned} f_i(\mathbf{x}+\mathbf{e}_i\Delta t, t+\Delta t) = f_i(\mathbf{x}, t) &- \frac{1}{\tau_{\mathrm{NS}}^{+}}\left(f_i^{+}(\mathbf{x}, t) - f_i^{\mathrm{eq}+}(\mathbf{x}, t)\right) \\ &- \frac{1}{\tau_{\mathrm{NS}}^{-}}\left(f_i^{-}(\mathbf{x}, t) - f_i^{\mathrm{eq}-}(\mathbf{x}, t)\right); \end{aligned} \tag{4}$$

$$f_i^{\pm} = \frac{f_i \pm f_{\bar{i}}}{2}, \qquad f_i^{\mathrm{eq}\pm} = \frac{f_i^{\mathrm{eq}} \pm f_{\bar{i}}^{\mathrm{eq}}}{2}. \tag{5}$$

Here, $\bar{i}$ is the direction opposite to $i$, that is, $\mathbf{e}_{\bar{i}} = -\mathbf{e}_i$. The values of $\tau_{\mathrm{NS}}^{+}$ and $\tau_{\mathrm{NS}}^{-}$ are defined as

$$\nu = c_s^2\left(\tau_{\mathrm{NS}}^{+} - \frac{1}{2}\right), \qquad \Lambda^{\pm} = \left(\tau_{\mathrm{NS}}^{\pm} - \frac{1}{2}\right) \tag{6}$$

from the viscosity of the fluid $\nu$ and $\Lambda = \Lambda^{+}\Lambda^{-}$, the product of the two eigenvalue functions $\Lambda^{+}$ and $\Lambda^{-}$. This product characterizes the numerical truncation error and stability of the TRT model. In the following, $\Lambda = \frac{3}{16}$, if not specified otherwise. This value ensures that walls implemented via the bounce-back scheme are located exactly halfway between a solid and a fluid node. Other values can cancel higher order spatial errors, or ensure resilient simulation (Ginzburg et al., 2008; d'Humières & Ginzburg, 2009; Khirevich et al., 2015).

### 2.1.2. Advection-Diffusion Equations

Advection and diffusion (AD) of a scalar field are described in a similar manner as the hydrodynamic equations given by Equation 1. In the following, AD populations are indicated by $g_i$.

$$g_i(\mathbf{x}+\mathbf{e}_i\Delta t, t+\Delta t) = g_i(\mathbf{x}, t) - \frac{1}{\tau_{\mathrm{AD}}}\left(g_i(\mathbf{x}, t) - g_i^{\mathrm{eq}}(\mathbf{x}, t)\right). \tag{7}$$

Here, $\tau_{\mathrm{AD}}$ is determined by the diffusivity of the scalar $\mathrm{D} = c_s^2(\tau_{\mathrm{AD}} - 0.5)$ and $g_i^{\mathrm{eq}}$ is

$$g_i^{\mathrm{eq}}(C, \mathbf{u}) = C\mathrm{w}_i\left[1 + \frac{\mathbf{u}\cdot\mathbf{e}_i}{c_s^2}\right]. \tag{8}$$

Here, $\mathbf{u}$ is the local advection velocity of the corresponding fluid field (cf. Equation 3). From Equation 7, the concentration $C$ of the scalar field is determined as

$$C = \sum_i g_i. \tag{9}$$

Note, that using this local advection velocity, the first moment of $g_i$, that is, momentum, is not conserved. Therefore, Equation 7 solves only the AD equation but not the NS equations (cf. Equation 1). With fewer degrees of freedom, it is sufficient to use a reduced D2Q5 lattice (cf. Appendix A) and a linear equilibrium function (cf. Equation 8) to solve Equation 7 which significantly decreases computational efforts.

The scalar field can also be solved using the TRT collision operator, for both accuracy and stability reasons. The corresponding set of equations reads

$$\begin{aligned} g_i(\mathbf{x} + \mathbf{e}_i\Delta t, t + \Delta t) = g_i(\mathbf{x}, t) &- \frac{1}{\tau_{\mathrm{AD}}^{-}}\left(g_i^{+}(\mathbf{x}, t) - g_i^{\mathrm{eq}+}(\mathbf{x}, t)\right) \\ &- \frac{1}{\tau_{\mathrm{AD}}^{+}}\left(g_i^{-}(\mathbf{x}, t) - g_i^{\mathrm{eq}-}(\mathbf{x}, t)\right) \end{aligned} \tag{10}$$

$$g_i^{\pm} = \frac{g_i \pm g_{\bar{i}}}{2}, \qquad g_i^{\mathrm{eq}\pm} = \frac{g_i^{\mathrm{eq}} \pm g_{\bar{i}}^{\mathrm{eq}}}{2}. \tag{11}$$

Analogous to the hydrodynamic equations, $\tau_{\mathrm{AD}}^{+}$ and $\tau_{\mathrm{AD}}^{-}$ depend on both the diffusivity and the product of the two eigenvalues $\Lambda^{+}$ and $\Lambda^{-}$. By default, $\Lambda = \frac{3}{16}$ for the same reasons as stated in the hydrodynamic equations.

$$D = c_{\mathrm{s}}^2\left(\tau_{\mathrm{AD}}^{+} - \frac{1}{2}\right), \qquad \Lambda^{\pm} = \left(\tau_{\mathrm{AD}}^{\pm} - \frac{1}{2}\right). \tag{12}$$

### 2.2. Rest Fraction Method

Coupling NS and AD via the advection velocity requires the same spatial and temporal discretization of both fields. Together with the two facts that (a) $\tau_j$ should be within the range of $\tau_j \approx [0.6, 1.4]$ to ensure numerical stability and accuracy (He et al., 1997; Krüger et al., 2017, p. 188) and (b) $\tau_j$ is proportional to $\nu$ or D (and therefore also to the Reynolds or Péclet number) this strongly limits the range of applicable Reynolds-to-Péclet ratios.

Using the TRT method where $\tau_j \approx [0.6, 4.0]$ can slightly extend this range. However, a technique to significantly increase the range is the rest fraction method. It decouples the discretization and relaxation time by redefining the equilibrium function of the scalar field (Sullivan, Johns, et al., 2005; Sullivan, Sani, et al., 2005). Following (Looije et al., 2018), here, the original formulation is interpreted as a method to change $c_{\mathrm{s}}^2$ as well as the weights $\mathrm{w}_i$ by the rest fraction $J_0$

$$\mathrm{w}_i\,(J_0) = \begin{cases} J_0 & \text{if} \quad i = 0, \\ c_{\mathrm{s}}^2/2 & \text{otherwise;} \end{cases} \tag{13}$$

$$c_{\mathrm{s}}^2 = \frac{1 - J_0}{\mathrm{dim}}, \tag{14}$$

where "dim" is 2 for D2Q5 and 3 for D3Q7. This approach does not affect the other equations, that is, Equations 1–12, unlike the original formulation. Note that setting the free parameter $J_0 = 1/3$ for D2Q5 or $J_0 = 1/4$ for D3Q7 results in the commonly used values for $c_{\mathrm{s}}^2$ and $\mathrm{w}_i$.

The rest fraction method allows for tuning the relation between diffusivity and relaxation time, with $\mathrm{D} = \frac{(1-J_0)}{\mathrm{dim}}(\tau_{\mathrm{AD}} - 0.5)$. Therefore, Reynolds-to-Péclet ratios of up to 1,000 can be achieved by adjusting solely $J_0$, while keeping $\tau \approx 1$.

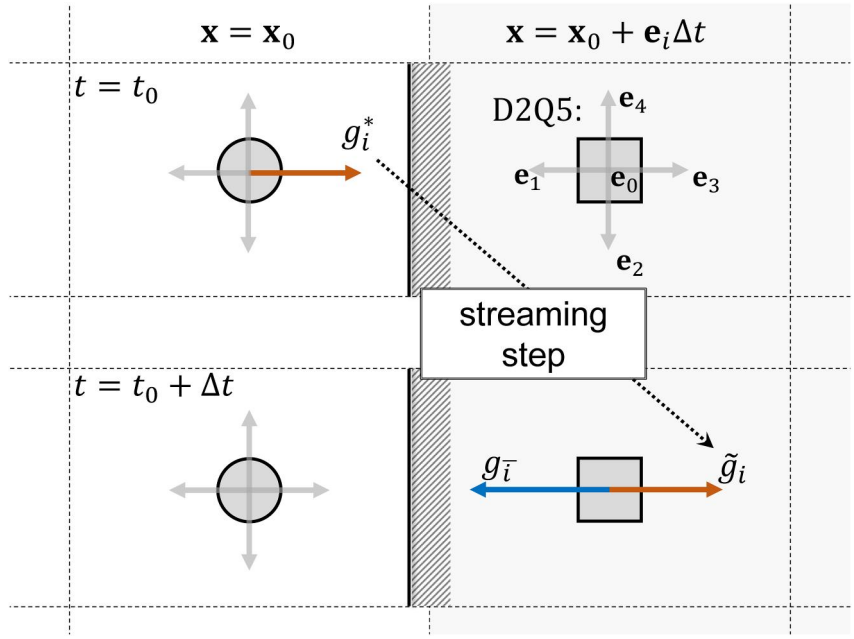


**Figure 1.** Schematic representation of the first-order RBC. Fluid nodes (circles) are depicted on the left side. Solid nodes (squares) are depicted on the right side. The top and the bottom rows only differ in time, but not in space. The streaming of population $g_i^* = g_i(\mathbf{x},\ t_0)$ to $\tilde{g}_i = g_i(\mathbf{x} + \mathbf{e}_i\Delta t,\ t_0 + \Delta t)$ are indicated by the orange arrows; the result of the RBC $g_{\bar{i}} = g_{\bar{i}}(\mathbf{x} + \mathbf{e}_i\Delta t,\ t_0 + \Delta t)$ with the blue arrow. In addition, the top right quadrant shows the D2Q5 velocity set ($\mathbf{e}_i$ for $i \in \{0, 1, 2, 3, 4\}$).

### 2.3. Reactive Boundary Conditions

All RBC schemes discussed in this paper macroscopically describe a first-order equilibrium reaction given as

$$J_\mathrm{R} = k_\mathrm{r}(C_\mathrm{eq} - C_\mathrm{wall}). \tag{15}$$

Here, $J_\mathrm{R}$ is the reaction rate, interpretable as a population flux. $k_\mathrm{r}$ is the reaction rate coefficient and $C_\mathrm{eq}$ and $C_\mathrm{wall}$ are the equilibrium concentration and concentration at the wall, respectively. The AD scalar field can also represent temperature, in which case the population flux $J_\mathrm{R}$ describes a heat flux, instead of a reaction.

The macroscopic flux $J_\mathrm{R}$ cannot be directly used in LBM due to its mesoscopic character, where the flux is determined using the populations. In addition, $C_\mathrm{wall}$ is unknown and needs to be estimated using an appropriate mesoscopic scheme. Details of how to transform the macroscopic first-order equilibrium reaction (cf. Equation 15) into a mesoscopic boundary condition (cf. Equation 16) are given in Text S1.1 in Supporting Information S1.

Figure 1 schematically shows the functioning principle of the set of RBC schemes discussed in this paper. It starts with the population $g_i^* = g_i(\mathbf{x},\ t_0)$ pointing toward the wall and before streaming. After streaming this population becomes $\tilde{g}_i = g_i(\mathbf{x} + \mathbf{e}_i\Delta t,\ t_0 + \Delta t)$. The actual main step of the RBC scheme determines the unknown population $g_{\bar{i}}$ from the known $\tilde{g}_i$. For the next streaming step $g_{\bar{i}}$ is required, and it is the final outcome of an RBC scheme.

The RBC schemes of Verhaeghe et al. (2006), Patel (2016) and Ju et al. (2020), and the new RBC scheme are presented in the following. For brevity, in the following only the first authors are mentioned and the corresponding schemes are abbreviated to S.V., S.P.J. and S.New, respectively. For comparability they are reformulated to a similar notation.

It is shown in detail in Supporting Information S1 (cf. Text S1) that they can be expressed in the form

$$g_{\bar{i}} = \frac{k_i}{1+k_i} 2 w_i C_{eq} + \frac{1-k_i}{1+k_i} \tilde{g}_i. \tag{16}$$

The difference of the schemes only enters by the definition of the term $k_i$

$$k_i^{(S.V.)} = c_s^{-2} \quad k_r \cdot (\mathbf{e}_{\bar{i}} \cdot \mathbf{n}) \tag{17}$$

$$k_i^{(S.P.J.)} = c_s^{-2} \gamma k_r / \ (\mathbf{e}_{\bar{i}} \cdot \mathbf{n}) \tag{18}$$

$$k_i^{(S.New)} = c_s^{-2} \gamma k_r \cdot (\mathbf{e}_{\bar{i}} \cdot \mathbf{n}), \tag{19}$$

and more specifically by the incorporation of the wall normal term $(\mathbf{e}_{\bar{i}} \cdot \mathbf{n})$ and the correction factor $\gamma = \tau_{AD} / (\tau_{AD} - 0.5)$. This reformulation approach also allows cross-implementation of already developed features from one RBC to the other, for example, moving walls. Here, it is used to highlight the differences of the schemes.

In the scheme of Verhaeghe the wall normal term is included in the numerator and $\gamma$ is not considered. In the schemes of Patel and Ju the wall normal term is included in the denominator and $\gamma$ is considered. Compared to the scheme of Verhaeghe, in the schemes of Patel and Ju the $\gamma$ can be interpreted as a shift in the effective reaction rate. The novel scheme proposed here is only slightly different and combines elements from both the scheme of Verhaeghe and the schemes of Patel and Ju. This, however, significantly improves both accuracy and applicability for complex geometries, and overcomes the $\tau$-dependent wall diffusion as is shown in Section 3.

For all three schemes, the limits of the reaction rate are similar (Ju et al., 2020; Patel, 2016; Verhaeghe et al., 2006): At high reactivity ($k_r \to \infty$), the schemes simplify to the anti bounce-back scheme (anti-BB) $g_{\bar{i}} = 2 w_i C_{eq} - \tilde{g}_i$, which sets the wall concentration to the equilibrium concentration. If no reactions occur ($k_r = 0$), the schemes simplify to the common bounce-back method, that is, $g_{\bar{i}} = \tilde{g}_i$.

### 2.4. Dissolution and Precipitation

Finally, simulating phase changes such as dissolution and precipitation at solid surfaces is built up on the RBC scheme. After the determination of the reaction flux using the RBC scheme, the flux enters a method that determines the amount of phase being changed as well as the direction of this process. In this paper, the so-called adjacent growth method (Kang & Lichtner, 2013; Kang et al., 2010) is used. It keeps track of the solid fraction $\phi$ for each cell during the simulation, where the change of $\phi$, that is, $\Delta\phi$, is determined as

$$\Delta\phi = V_m a_m \left( \sum_i g_{\bar{i}} - \tilde{g}_i \right) \Delta t. \tag{20}$$

Here, $V_m$ is the dimensionless molar volume and $a_m$ is the specific surface area. The summation term represents the reaction flux determined from the RBC scheme (cf. Figure 1). In this study and as proposed by Kang et al. (2006), $\Delta t = 1$ and $a_m = 1$ are used.

During the run time of the simulation $\phi$ is dynamically updated. If $\phi$ in a cell exceeds a certain threshold, the phase type of this cell is changed from solid to fluid for dissolution, or vice versa for precipitation. In this study, threshold values of Kang et al. (2006) and Pedersen et al. (2014) are used. They used $\phi = 0$ for dissolution and $\phi = 1$ for precipitation. This mimics a phase change hysteresis. For precipitation, the local concentration is converted to $\phi$ and any excess is distributed to the surrounding fluid cells. The amount being distributed is weighted by the reaction rate of the cell. For dissolution, an initial concentration equal to the average concentration of the surrounding fluid cells is set and an the corresponding amount of $\phi$ is removed from the surrounding solid cells.

## 3. Results

The RBC schemes of Verhaeghe, Patel and Ju, and the new scheme are compared and verified using a variety of simulation tests. These concern the accuracy of the schemes using a robust 2D reaction-diffusion verification case

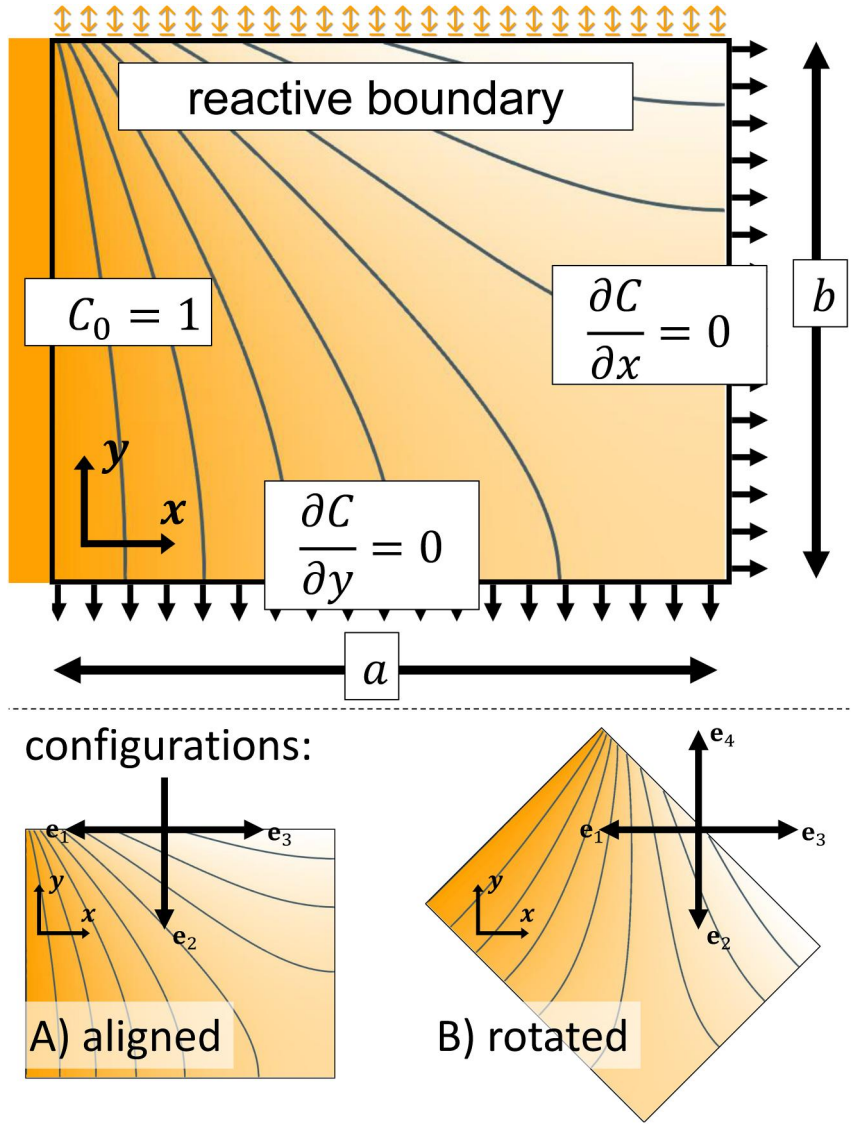


**Figure 2.** Simulation setup of the 2D reaction-diffusion problem. The boundary conditions are constant concentration (left), zero concentration gradient (right and bottom), and first-order equilibrium reaction (top). An exemplary concentration field and its analytical solution are indicated by the background and the contour lines, respectively. Two variants of this setup are studied; one where the boundaries are aligned with the D2Q5 grid (configuration A) and another which is rotated clockwise by a 45° angle (configuration B).

with analytical solution, pattern formation during precipitation, and an encompassing case study with a reactive circular object inside a channel flow proposed by Molins et al. (2020).

The different simulation tests are conducted for a broad range of advection, diffusion, and reaction regimes. They are characterized by the non-dimensional Reynolds (Re), Péclet (Pe), Damköhler (Da), and Péclet-Damköhler (PeDa) number, which are given as

$$\mathrm{Re} = \frac{\mathrm{U\,L}}{\nu}, \qquad \mathrm{Pe} = \frac{\mathrm{U\,L}}{\mathrm{D}}, \qquad \mathrm{Da} = \frac{k_\mathrm{r}}{\mathrm{U}}, \qquad \mathrm{PeDa} = \frac{k_\mathrm{r}\mathrm{L}}{\mathrm{D}}. \tag{21}$$

Here, U and L are the characteristic velocity and length, respectively. Note that the Péclet-Damköhler number, which opposes reaction and diffusion rates, defines the behavior of pure reaction-diffusion problems. For PeDa $\to \infty$ diffusion is limiting and for PeDa $\to 0$ it is reaction.

**Table 1**
*Parameter Set for the 2D Reaction-Diffusion Case*

| Parameter | | Value | Unit |
|---|---|---|---|
| Width | $a$ | 100 | lm |
| Height | $b$ | 80 | lm |
| Péclet number | Pe | 1 | – |
| Inlet concentration | $C_0$ | 1 | lc |
| Equilibrium concentration | $C_{eq}$ | 0 | lc |
| Resolution | N | 80 | lm |
| Lattice velocity | U | 0.001 | lm ls$^{-1}$ |

### 3.1. Analytical Reaction-Diffusion Verification

A simple 2D reaction-diffusion problem is studied, for which also an analytical solution exists (cf. Equation 22). The corresponding simulation setup is shown in Figure 2. The bulk is solved using the BGK collision operator. The simulation considers pure diffusion of a concentration field within a rectangular domain, thus $\mathbf{u} = 0$. At the left boundary, a constant concentration $C_0$ is defined. The bottom and right boundaries are set to $\nabla C = 0$. At the top boundary a first-order equilibrium reaction is modeled using either the scheme of Verhaeghe, the schemes of Patel and Ju, or the new scheme.

The analytical solution to this problem (Carslaw & Jaeger, 1986, p. 167) using the formulation of Kang et al. (2006) is

$$C^{(\text{analyt})}(x,y) = (C_0 - C_{eq}) \sum_{n=1}^{\infty} \left( \frac{\sin(\beta_n b)}{N_n^2 \beta_n} \frac{\cosh(\beta_n (x-a))}{\cosh(\beta_n a)} \cdot \cos(\beta_n y) \right) + C_{eq}, \tag{22}$$

where $C^{(\text{analyt})}(x, y)$ is the local analytical concentration, $C_{eq}$ the equilibrium concentration at the top boundary, and $a$ and $b$ are the width and height, respectively. In this paper, the sum in Equation 22 is evaluated up to $n = 100$. The parameters $N_n^2$ is given as

$$N_n^2 = \frac{b}{2}\left(1 + \frac{\sin(2\beta_n b)}{2\beta_n b}\right), \tag{23}$$

and $\beta_n$ are the solutions to the following transcendental

$$(\beta_n b)\tan(\beta_n b) = \frac{k_r b}{D} = \text{PeDa}. \tag{24}$$

Simulations are conducted for PeDa numbers in the range of PeDa = $[10^{-1}, 10^5]$ and for the two different configurations shown in Figure 2: (a) Configuration A with walls that are perfectly aligned with the grid orientation. (b) Configuration B in which the setup is rotated by 45° with respect to the grid. This enables the isolated analysis of the correction factor $\gamma$ and the impact of the wall normal term $(\mathbf{e}_{\bar{i}} \cdot \mathbf{n})$ on the simulation result.

The accuracy of the simulations, that is, the deviation of the simulation data and the analytical solution, is quantified using the mean absolute error (MAE)

$$\text{MAE} = \sum_{x=0}^{a} \sum_{y=0}^{b} \left| C^{(\text{sim})}(x,y) - C^{(\text{analyt})}(x,y) \right|. \tag{25}$$

If not stated otherwise, the values given in Table 1 are used for the simulation. Values are given in non-dimensional units, that is, lattice meter [lm], lattice second [ls], and lattice concentration [lc]. The value of PeDa is varied by changing the Da number only, while keeping $\tau_{AD}$ constant in all simulations.

#### 3.1.1. Configuration A: Aligned System

In configuration A, the term $\mathbf{e}_i \cdot \mathbf{n}$ in Equations 17–19 simplifies to 1 for $\mathbf{e}_2$ pointing toward the simulation domain, and 0 otherwise. Thus, the implementation of the wall normal does not affect $k_i$ (cf. Equation 17–19) such that the schemes of Patel and Ju, and the new scheme are identical; only the scheme of Verhaeghe differs by the factor $\gamma$.

The simulation results of the concentration field are shown in Figure 3 for PeDa = 1 and PeDa = 100. The colors show the concentration. The analytical solution is depicted by the black contour lines for the distinct values given in the plot. In addition, the corresponding absolute error is shown in Figure 4.

10.1029/2023WR034770

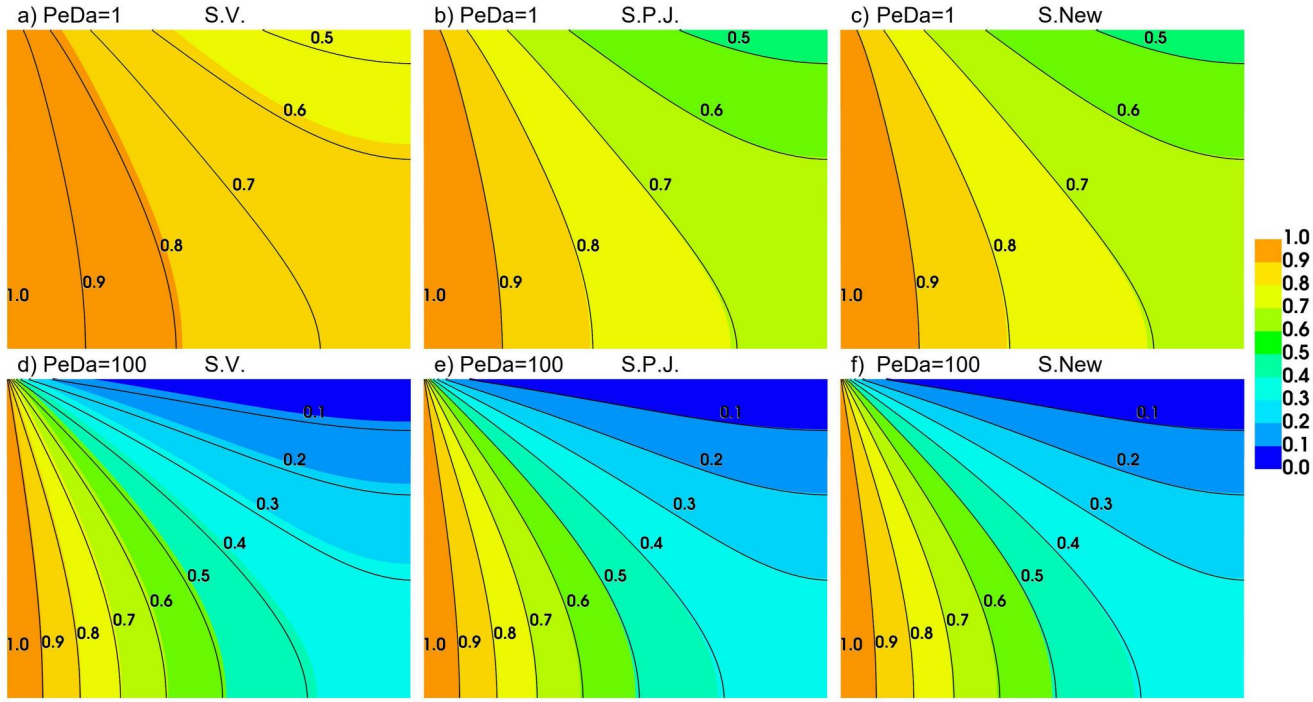


**Figure 3.** Simulation results of configuration A of the reaction-diffusion problem using the schemes of Verhaeghe (S.V.), Patel and Ju (S.P.J.), and the new scheme (S. New) for PeDa = 1 and PeDa = 100. The concentration field is shown by the color code given in the legend. The analytical solution (cf. Equation 22) is indicated by the black contour lines for the distinct values given in the plot.

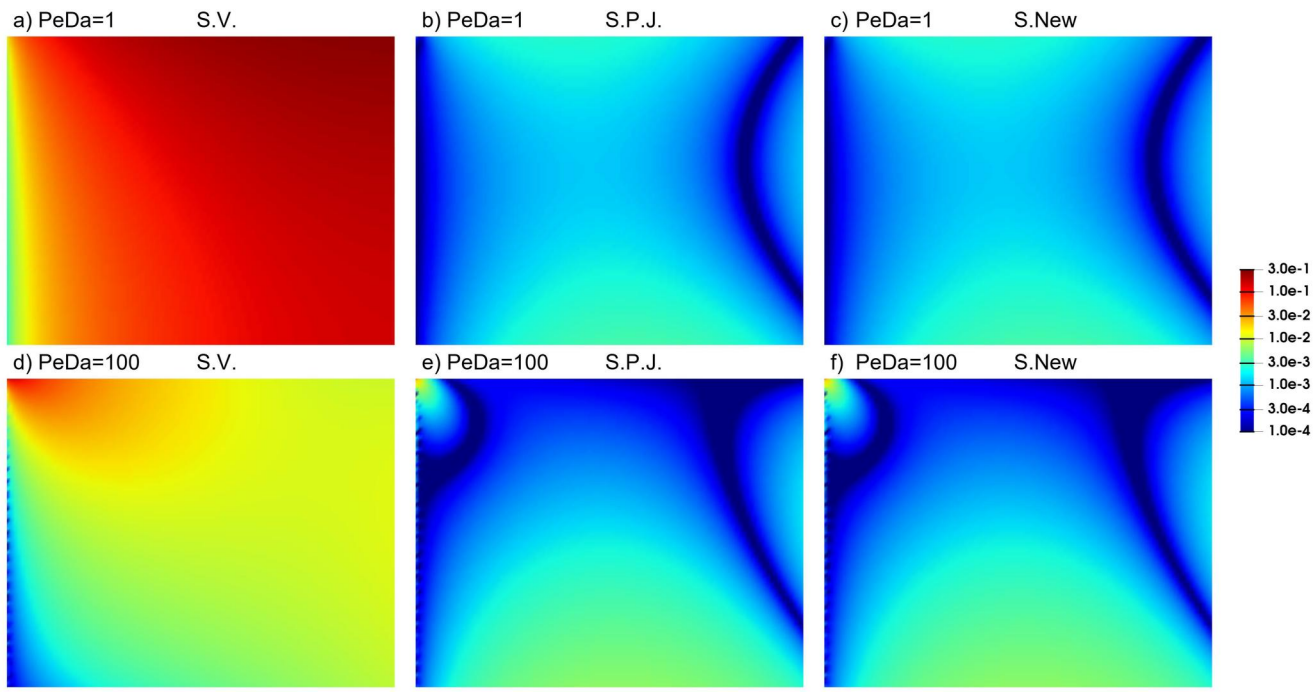


**Figure 4.** Absolute error of configuration A of the reaction-diffusion simulations using the schemes of Verhaeghe (S.V.), Patel and Ju (S.P.J.), and the new scheme (S. New) for PeDa = 1 and PeDa = 100. The error is shown by the color code given in the legend.

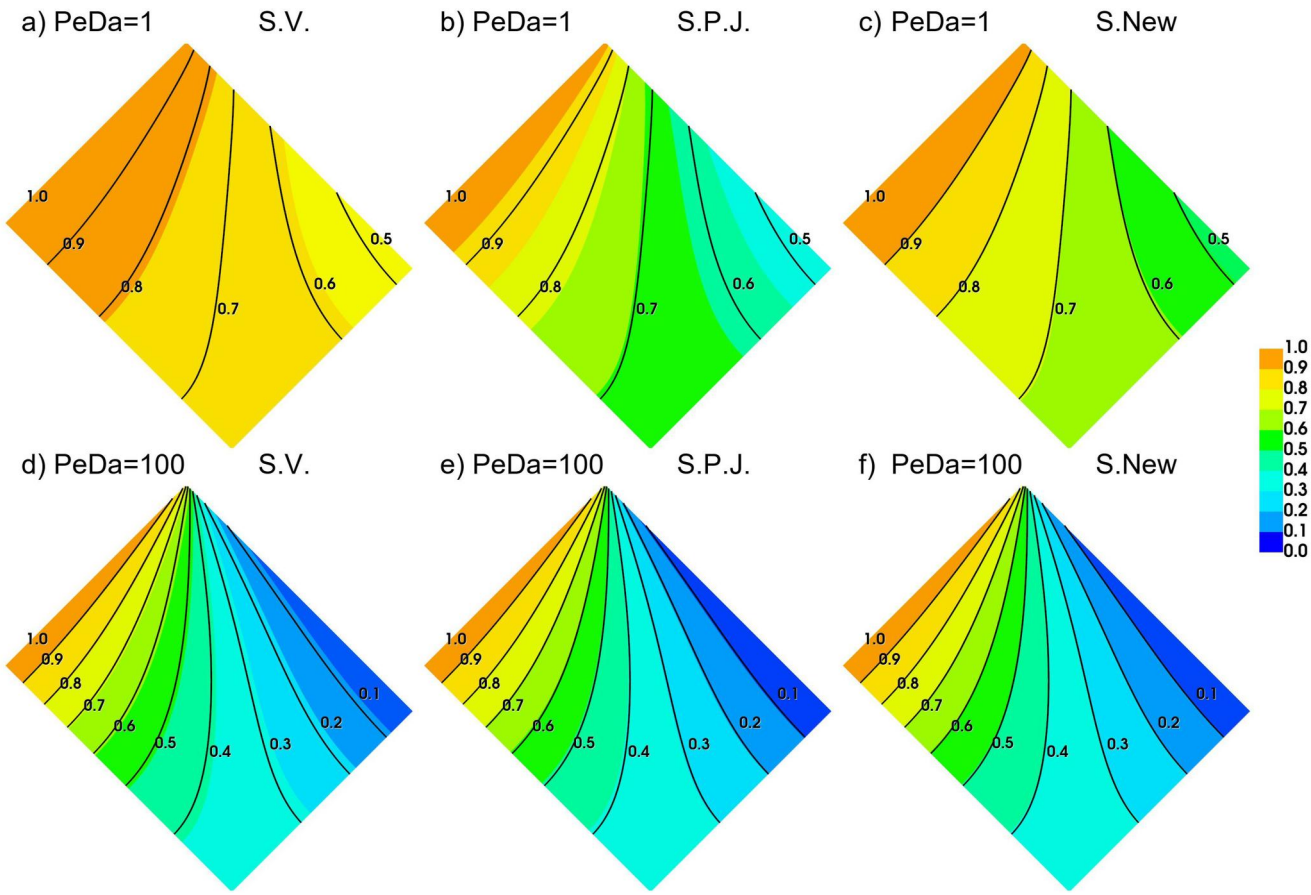


**Figure 5.** Simulation results of configuration B of the reaction-diffusion problem using the schemes of Verhaeghe (S.V.), Patel and Ju (S.P.J.), and the new scheme (S. New) for PeDa = 1 and PeDa = 100. The concentration field is shown by the color code given in the legend. The analytical solution (cf. Equation 22) is indicated by the black contour lines for the distinct values given in the plot.

For the predominantly diffusion-limited case (PeDa = 100), shown in Figures 3 and 4d–4f, all RBC schemes are at least in good agreement with the analytical solution. While for the scheme of Verhaeghe the absolute error is $<10^{-2}$ over large areas of the simulation domain, the schemes of Patel and Ju, and the new scheme are even more accurate (absolute error $<10^{-3}$). This is, however, different for the predominantly reaction-limited case (PeDa = 1), shown in Figures 3 and 4a–4c. There, the scheme of Verhaeghe shows a significant deviation from the analytical solution, while the schemes of Patel and Ju, and the new scheme are again in almost perfect agreement with the analytical solution.

For configuration A, the difference from the scheme of Verhaeghe compared to the schemes of Patel and Ju, and the new scheme is solely attributed to the absence of $\gamma$. As described in the literature (Ju et al., 2020; Patel, 2016), including $\gamma$ ensures that the macroscopic diffusivity at the wall is captured correctly. Multiplying the PeDa number in Equation 24 by a factor of $1/\gamma$ results in no error when using the scheme of Verhaeghe, confirming the shift in effective PeDa number simulated.

Additionally, this setup is used to confirm that integrating RBC with the rest fraction method and TRT collision operator is valid. The resultant MAE increase is less than 1% (cf. Text S2 in Supporting Information S1), and thus does not result in significant additional errors.

### 3.1.2. Configuration B: Rotated System

In configuration B, primarily the influence of the wall normal on $k_i$ (cf. Equation 17−19) is tested. The simulation setup is similar to configuration A, with the only difference that it is rotated clockwise by 45°. This leads to the term $\mathbf{e}_i \cdot \mathbf{n}$ in Equation 17−19 being equal to $-\sqrt{2}/2$ for $\mathbf{e}_{1,2}$, that is, pointing toward the simulation domain. Thus,

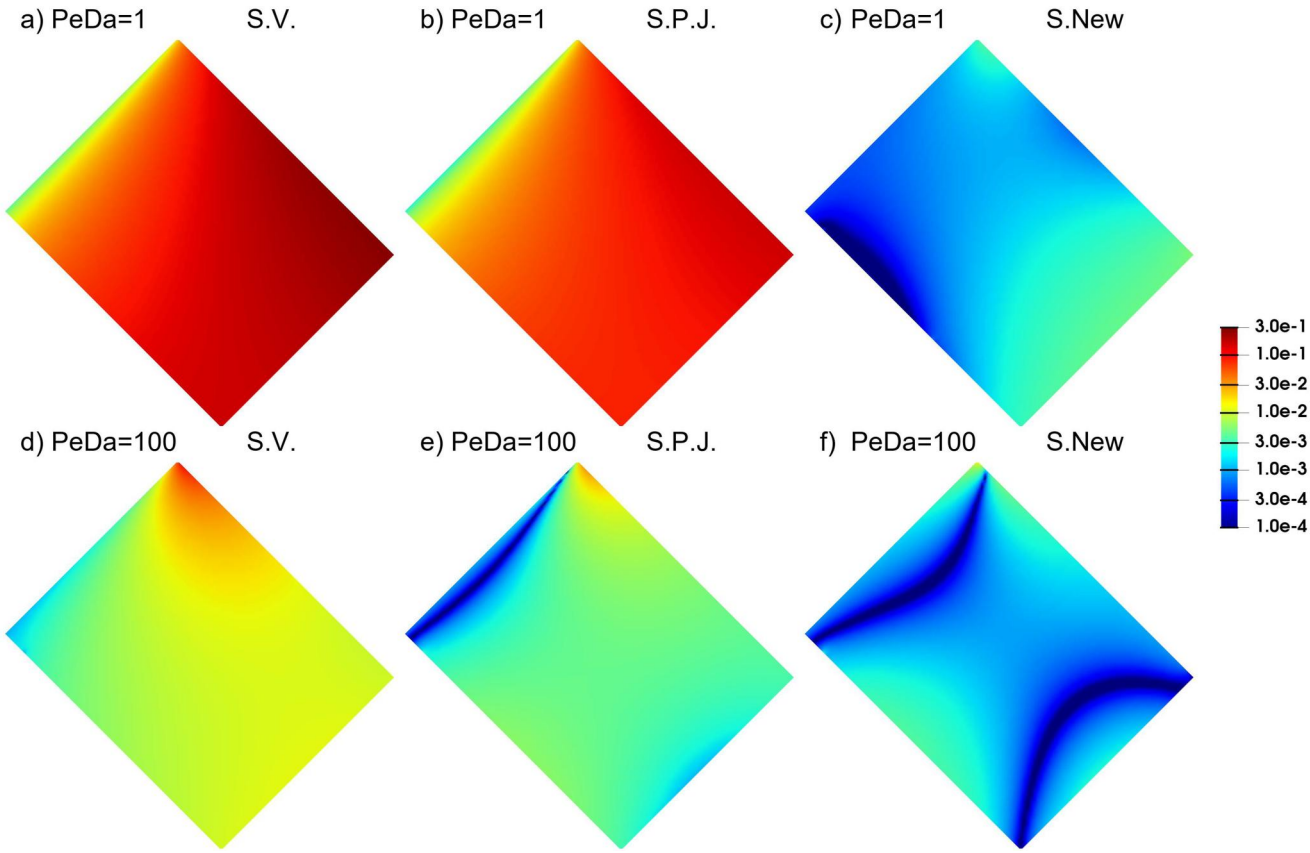


**Figure 6.** Absolute error of configuration A of the reaction-diffusion simulations using the schemes of Verhaeghe (S.V.), Patel and Ju (S.P.J.), and the new scheme (S. New) for PeDa = 1 and PeDa = 100. The error is shown by the color code given in the legend.

none of the three schemes compared here are identical anymore. Deviations from the configuration A predominately originate from the implementation of the wall normal.

Again, for PeDa = 1 and PeDa = 100, the simulation results and corresponding absolute error are shown in Figures 5 and 6, respectively. The meaning of the colors and lines is identical to those from Figures 3 and 4.

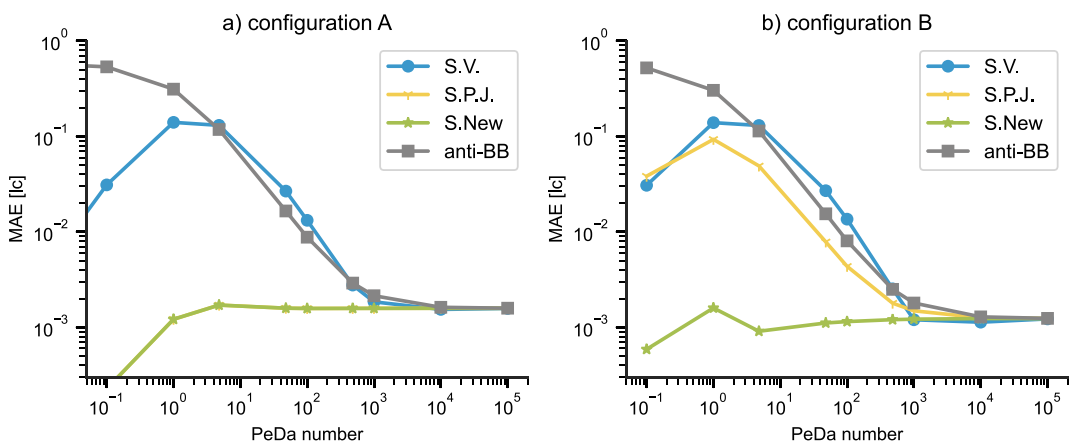


**Figure 7.** MAE analysis of configuration A and B of the reaction-diffusion simulations using the schemes of Verhaeghe (S. V.), Patel and Ju (S.P.J.), and the new scheme (S.New) with extended PeDa range ($10^{-1}$ to $10^{5}$). The MAE of the schemes of Patel and Ju, and the new scheme are identical for configuration A.

The simulation results of the scheme of Verhaeghe and the new scheme are similar to those from configuration A. Again, multiplying the PeDa number in Equation 24 by a factor of $1/\gamma$, to match the analytical PeDa to the simulated PeDa, results in no error of the scheme of Verhaeghe. However, a large deviation from the analytical solution is observed for the schemes of Patel and Ju especially at low PeDa values.

#### 3.1.3. Configuration A and B for Extended PeDa Range

The MAE (cf. Equation 25) of the RBC schemes are summarized in Figure 7 for both configuration A and B over a vast range of PeDa values. When PeDa $\to \infty$, the RBC schemes approach the anti-BB method. This was shown in the literature (Ju et al., 2020; Verhaeghe et al., 2006) and is further elaborated in Text S1.3 in Supporting Information S1. Note, that the anti-BB sets the equilibrium concentration at the boundary. Therefore, this approximation is expected to have significant errors at low PeDa values. Still, it is included as reference in the extended MAE plots.

For configuration A (cf. Figure 7a), it clearly shows how the scheme of Verhaeghe has significant errors for $10^{-1} \lesssim \text{PeDa} \lesssim 10^{2}$, with an decreasing error for when PeDa $\to \infty$. On the other hand, the schemes of Patel and Ju, and the new scheme are barely affected by the choice of PeDa. This highlights the impact of $\gamma$. The MAE decreases for all schemes in the reaction-limited case, that is, PeDa $< 1$, which has the trivial solution of $C(x, y) = C_0$, with the RBC approaching bounce-back behavior.

For configuration B (cf. Figure 7b), the scheme of Verhaeghe and the new scheme behave the same as in configuration A (cf. Figure 7a). However, the scheme of Patel and Ju shows a significant error, due to their wall-normal implementation. In contrast, the new scheme developed in the current study, is almost not affected by the choice of PeDa for both configuration A and B.

The MAE values for RBC and anti-BB schemes converge for PeDa $> 10^3$ in configuration A and for PeDa $> 10^4$ in configuration B. Thus, simulations with PeDa $> 10^4$ show similar results for all aforementioned RBC schemes, that is, anti-BB, the schemes of Verhaeghe, Patel and Ju, and the new scheme.

### 3.2. Pattern Formation During Precipitation

This test case is motivated by the work of Pedersen et al. (2014). They investigated pattern formation of grain growth during precipitation and its dependence on the grid orientation. For their study they used the scheme of Verhaeghe.

The simulation domain is circular with a diameter of 300 grid cells. This is realized by adding boundary cells along this circle in a square domain of size 300 lm $\times$ 300 lm cells. On the boundary the concentration is constant, that is, $C_{\text{circ}} = 1$. An initial seed is placed in the center of the domain. Its shape is defined by the parametric equation

$$\begin{aligned} x(s) &= [0.1 + 0.02\cos(8\pi s)]\cos(2\pi s), \\ y(s) &= [0.1 + 0.02\cos(8\pi s)]\sin(2\pi s), \end{aligned} \tag{26}$$

with $s$ as the parameter. Two variants of this setup are simulated: One where the initial seed is aligned with the grid orientation, and another where the initial seed is rotated clockwise by 19°. The boundaries of the seed are defined by a RBC with $C_{\text{eq}} = 0$ and $k_{\text{r}} = 0.0014$ (cf. Equation 16). The bulk is solved using the BGK collision operator. Pure diffusion is considered such that $\mathbf{u} = 0$ within the domain. To compute the wall normal, the simple and efficient isotropic finite difference method (Kumar, 2004) is used.

The results determined with the scheme of Verhaeghe, the schemes of Patel and Ju, and the new scheme are shown in Figure 8. The resulting patterns when using the scheme of Verhaeghe and the new scheme are similar, as shown in Figures 8a, 8d and 8c, 8f, respectively. However, for the scheme of Verhaeghe the growth is less pronounced which is due to the effective PeDa shift. A correction of this shift further improves the accordance of both schemes. In contrast, the pattern resulting from the schemes of Patel and Ju shows dendritic behavior and grid dependence, shown in Figures 8b and 8e. The reason is due to the implementation of the wall normal in $k_i^{(\text{S.P.J.})}$ (cf. Equation 18), leading to faster reactions in diagonal walls compared to straight walls.

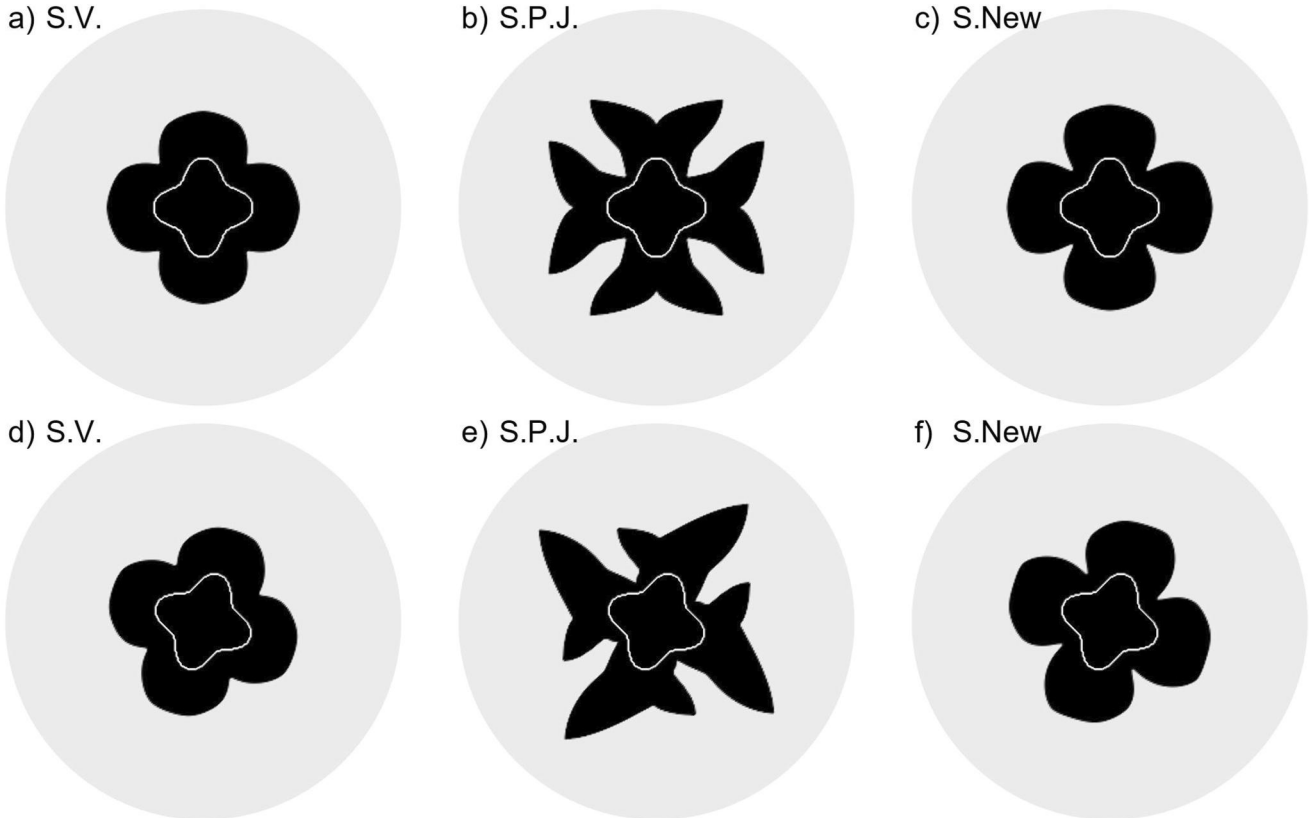


**Figure 8.** Pattern formation during precipitation using the schemes of Verhaeghe (S.V.), Patel and Ju (S.P.J.), and the new scheme (S.New) for PeDa = 10. The final grains are shown in black. The initial grain seeds and the simulation domain are indicated by the white line and the gray-shaded background, respectively.

### 3.3. Reaction in a Channel Flow

This case study considers a reactive object in a channel flow, that is, under the influence of advection. It is motivated by the extensive comparison paper by Molins et al. (2020) in which they compared five different simulation methods (Chombo-Crunch, dissolFoam, LBM, OpenFoam, and Vortex). Both Molins et al. (2020) and Ju et al. (2020) used the same dissolution experiment of Soulaine et al. (2017) to validate their methods.

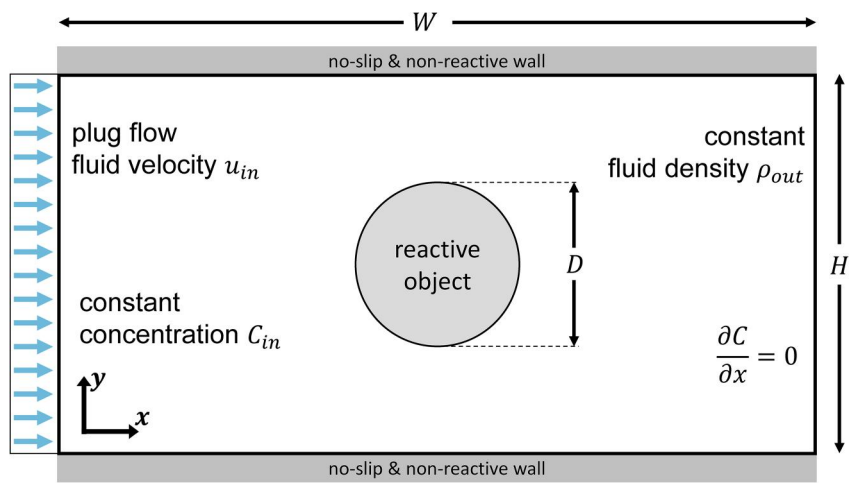


**Figure 9.** Simulation setup of the 2D reactive object in channel flow from Molins et al. (2020). The boundary conditions for (1) the fluid lattice are constant plug flow (left), constant density (right) and bounce-back walls (top, bottom, object), and for (2) the scalar lattice are constant concentration (left), zero concentration gradient (right), bounce-back walls (top, bottom) and RBC (object).

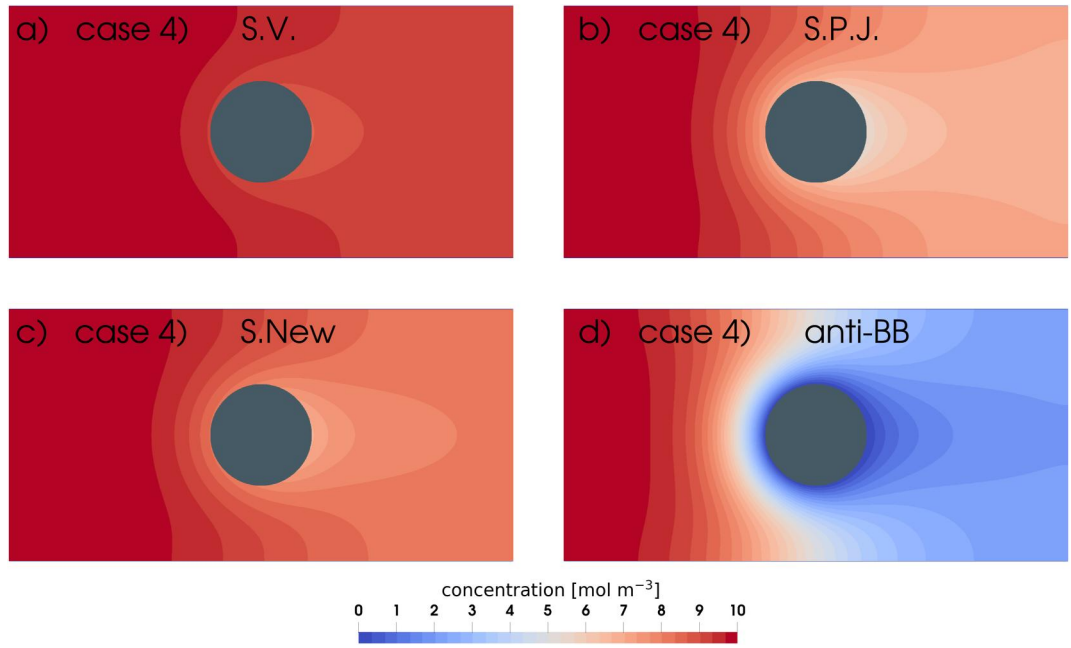


**Figure 10.** Concentration field in the vicinity of a reactive object (gray circle) in a channel flow simulated for Case (4) with Pe = 6, Da = 0.178. Using (a) the scheme of Verhaeghe, (b) the schemes of Patel and Ju, (c) the new scheme, and (d) the anti-BB scheme, which sets the concentration to the equilibrium concentration. The concentration is shown by the color code given in the legend.

The simulation setup is shown in Figure 9. It is 2D and consists of a channel with height $H = 0.05$ cm and width $W = 0.1$ cm, simulated with resolution 600 lm × 1,200 lm and a lattice velocity of $U_{LB} = 0.001$ lm ls$^{-1}$. The channel is initially filled with a fluid at rest and with constant concentration equal to that of the inlet. A circular reactive object with diameter $D = 0.02$ cm is placed in the middle of the channel. The boundary conditions for the carrier fluid are (a) bounce-back walls at the top, bottom, and at the object's surface, (b) plug velocity profile $u_{in} = 0.12$ cm/s at the inlet on the left, and (c) fixed density $\rho_{out} = 1$ at the outlet on the right. The boundary conditions for the concentration field are (a) bounce-back walls at the top and bottom, (b) constant concentration at the inlet $C_{in} = 10$ mol/m$^3$, (c) zero concentration gradient at the outlet, and (d) a RBC at the object's surface. The RBC is varied between the three schemes and the anti-BB. Large ratios of Pe to Re are realized using the TRT collision operator and rest fraction method for the concentration lattice. The following values are chosen: $J_0 = 0.99$ for Pe = 600 and $J_0 = 1/3$ for Pe = 6. First, the flow of the carrier fluid, that is, the NS lattice, was simulated until steady state was achieved. Then, the concentration field, that is, the AD lattice, was solved and the average reaction rate of the object was determined as

$$R_{\text{avg}} = \frac{1}{\pi D}\left(\int_{\text{outlet}} C u_x \cdot dy - C_{in} u_{in} H\right). \tag{27}$$

Here the integral is performed on the outlet.

Simulations were conducted for Re = 0.6 and different combinations of Pe = [6, 600] and Da = [0.178, 17,800]. These are: Case (1) Pe = 600, Da = 178 (diffusion limited); Case (2) Pe = 600, Da = 17,800 (diffusion limited); Case (3) Pe = 6, Da = 178 (advection-diffusion limited); and Case (4) Pe = 6, Da = 0.178 (advection-reaction-diffusion limited). As is shown in the following, the Cases (1) to (3) are not suited to differentiate the schemes, since they are not reaction limited.

A qualitatively comparison of the results of Case 4) for the schemes is given in Figure 10. A comparison between the Cases (1) to (4) for the new scheme is shown in Figure S1 in Supporting Information S1. In Case (4) when using the scheme of Verhaeghe (cf. Figure 10a), the simulation is strongly reaction limited, as indicated by the high concentration around the object's surface. In contrast, the anti-BB scheme (cf. Figure 10d) shows the case

**Table 2**
*Results of* $R_{avg}$ *of a Reactive Object in a Channel Flow*

| Input | | | $R_{avg}$ [$10^{-8}$ mol/(cm$^2$·s)] | | | | |
|---|---|---|---|---|---|---|---|
| Case | Pe | Da | Molins et al. (2020) | $S_{Ve}$ | $S_{P.J.}$ | $S_{New}$ | Anti-BB |
| (1) | 600 | 178 | [4.18, 4.57] | 4.48 | 4.66 | 4.64 | 4.71 |
| (2) | 600 | 17,800 | [3.88, 4.79] | 4.70 | 4.70 | 4.70 | 4.71 |
| (3) | 6 | 178 | [58.6, 90.5] | 75.5 | 75.9 | 75.8 | 76.0 |
| (4) | 6 | 0.178 | N/A | 8.05 | 29.1 | 18.5 | 76.0 |

where reaction is not limiting at all. Both the new scheme and the schemes of Patel and Ju (cf. Figures 10b and 10c, respectively) fall between the two extremes.

The numerical results of $R_{avg}$ are given in Table 2 together with the values from Molins et al. (2020). There, ranges are given as different methods were used to determine $R_{avg}$ (cf. Text S3 in Supporting Information S1). Overall, the RBC schemes agree well with the results of Molins et al. (2020), where available, indicating good integration of the RBC schemes with the rest fraction method.

Table 2 shows that for the Cases (1) to (3), the simulations are not reaction limited, resulting in the RBCs behaving similar to the anti-BB. Thus, cases in which the PeDa $\geq$ 1,000 are not suited for validation of RBC schemes. The experiment of Soulaine et al. (2017) has a PeDa = 3,000. In Case (4), the reaction is not limiting anymore, as indicated by the much higher anti-BB result. Here, the result of the various RBC schemes diverge. Compared to the new scheme, the scheme of Verhaeghe underestimates and the schemes of Patel and Ju overestimates $R_{avg}$ by the significant factors of 0.43 and 1.6 respectively.

The capability of the new scheme to handle complex media is demonstrated in Figure 11. The simulation setup remains the same (cf. Figure 9), just with multiple objects. Alongside the concentration field, the velocity field is indicated using black arrows. Notably, the downstream particles have the familiar low concentration tail, whereas the upstream particles do not due to mixing of the flow. This demonstration showcases how the new RBC scheme is applicable to arbitrary geometries due to its *general* and *local* properties.

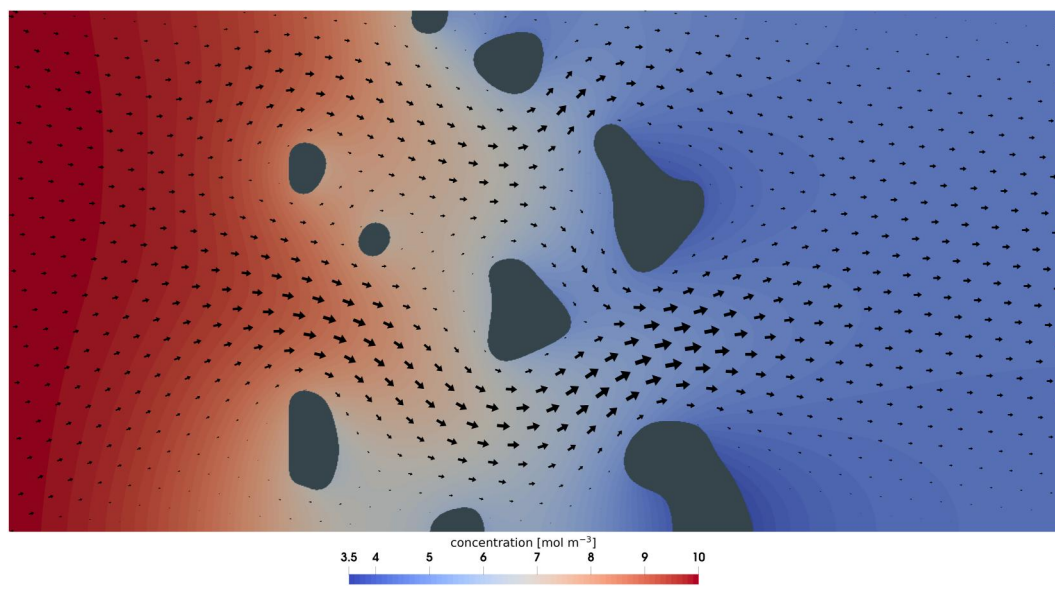


**Figure 11.** Concentration field in the vicinity of heterogeneous porous media in a channel flow simulated with Case (4) parameters with Pe = 6, Da = 0.178, using the new scheme. The concentration is shown by the color code given in the legend, and the velocity field is depicted using black arrows.

## 4. Conclusion

A new general local reactive boundary condition (RBC) scheme was presented that accurately captures first-order equilibrium reactions for a wide range of Péclet (Pe) and Damköhler (Da) numbers and is applicable to complex geometries. It combines aspects of previous RBCs from Verhaeghe et al. (2006), Ju et al. (2020), and Patel (2016), but overcomes their deficiencies. This means, the new RBC scheme does not suffer from a $\tau$-dependent wall diffusion and accurately considers the wall normal for complex geometries and surfaces that are not aligned with the simulation grid.

In this study, all aforementioned RBC schemes were first reformulated to a similar notation. Then, all RBC schemes were tested and compared using three different verification cases. These were chosen such that they were relevant, representative, and covered important features of RBCs and their applications: (a) A robust 2D reaction setup purely driven by diffusion. The problem has an analytical solution and the RBC schemes were studied over a wide range of PeDa values as well as under grid rotation. (b) Pattern formation in a precipitation process. Here, especially the impact of rotational variance and the behavior of the wall normal was studied. (c) An advanced reaction setup including advection around a reactive object in a channel flow. The RBC schemes were coupled to the rest fraction method, a wide range of PeDa values was studied, and the results were compared to results from the literature.

The test cases demonstrate a broad applicability and high accuracy of the new RBC scheme. For the 2D reaction setup, the new RBC scheme shows the best accordance with the analytical solutions. Additionally, it was shown that it correctly simulates wall diffusion and is invariant with respect to relaxation time and grid orientation. For the simple precipitation case, the new RBC scheme showed physically sound pattern formations. Moreover, in contrast to the other RBC schemes, it was not affected by grid rotation. For the advection case, large ratios of Péclet and Reynolds number ($\leq$1,000) were successfully simulated. Reaction rates determined using the new RBC scheme are in general accordance with results from the literature (Molins et al., 2020).

All in all, the new RBC accurately describes first-order reactions and can be applied to simulate precipitation and dissolution phenomena even for complex geometries. This is a strong advantage over other RBCs previously described in the literature. In addition, as a general and local scheme, it is easy to implement for both 2D and 3D simulations, it is computationally efficient and facilitates parallel computation. The new RBC scheme is missing some advanced features, for example, moving walls, or interpolated sub-grid wall locations. However, the presented general reformulation allows those already developed features to be incorporated easily.

The new RBC can be used to study reaction processes in a broad range of research fields. Potential applications might be reactive flows through porous media, with and without dissolution and precipitation (Jiang et al., 2021; Pereira, 2022; Xu et al., 2018; L. Zhang et al., 2019; D. Zhang et al., 2021; C. Zhang et al., 2021), pore structure evolution in cement manufacturing (Patel et al., 2021), or morphological changes due to the conversion of active material in energy storage systems (Fang et al., 2021). Especially the last topic will be in the focus of our future work.

## Appendix A: LBM Velocity Sets

This paper discusses the 2D implementation of the RBC only, as the extensions to 3D are simple and straightforward. The velocity sets used for the 2D implementations are D2Q9 and D2Q5 and are given in the following:

D2Q9

$$\begin{aligned}\{\mathbf{e}_i\} &= \{\mathbf{e}_0, \mathbf{e}_1, \mathbf{e}_2, \mathbf{e}_3, \mathbf{e}_4, \mathbf{e}_5, \mathbf{e}_6, \mathbf{e}_7, \mathbf{e}_8\} \\ &= \frac{\Delta x}{\Delta t}\begin{Bmatrix} 0 & -1 & -1 & -1 & 0 & 1 & 1 & 1 & 0 \\ 0 & 1 & 0 & -1 & -1 & -1 & 0 & 1 & 1 \end{Bmatrix}\end{aligned} \tag{A1}$$

$$\{\mathrm{w}_i\} = \left\{\frac{4}{9}, \frac{1}{36}, \frac{1}{9}, \frac{1}{36}, \frac{1}{9}, \frac{1}{36}, \frac{1}{9}, \frac{1}{36}, \frac{1}{9}\right\}$$

D2Q5

$$\{\mathbf{e}_i\} = \{\mathbf{e}_0, \mathbf{e}_1, \mathbf{e}_2, \mathbf{e}_3, \mathbf{e}_4\} = \frac{\Delta x}{\Delta t}\begin{Bmatrix} 0 & -1 & 0 & 1 & 0 \\ 0 & 0 & -1 & 0 & 1 \end{Bmatrix} \quad \{\mathrm{w}_i\} = \left\{\frac{1}{3}, \frac{1}{6}, \frac{1}{6}, \frac{1}{6}, \frac{1}{6}\right\} \tag{A2}$$

In both Equations A1 and A2 the speed of sound is $c_s = 1/\sqrt{3}\ \ \Delta \mathbf{x}/\Delta t$. When using the rest fraction method, both weights and speed of sound change (cf. Section 2.2).

## Data Availability Statement

An extended version of the **Par**allel **La**ttice **Bo**ltzmann **S**olver (version 2.3.0)—short Palabos—was used for all LBM simulations in this study. The original version of Palabos is preserved at https://palabos.unige.ch/, available via GNU Affero General Public License version 3 without login required and developed openly at https://gitlab.com/unigespc/palabos (Latt et al., 2021). The reactive boundary conditions and the rest fraction method were implemented separately.

**Acknowledgments**
The authors gratefully acknowledge financial support by the Federal Ministry of Education and Research (BMBF) within the project "SulForFlight" under the Grant 03XP0491A. M.L. and B.K. gratefully acknowledge financial support from the European Union's Horizon 2020 Research and Innovation Programme within the project "DEFACTO" under the Grant 875247. The simulations were carried out on the Hawk at the High Performance Computing Center Stuttgart (HLRS) under the Grant LaBoRESys, and on bwHPC JUSTUS 2 at the University Ulm under the Grant INST 40/467-1 FUGG. This work contributes to the research performed at CELEST (Center for Electrochemical Energy Storage Ulm-Karlsruhe). Open access funding enabled and organized by Projekt DEAL.

## References

Andrews, E. M., Hyman, J. D., Sweeney, M. R., Karra, S., Moulton, J. D., & Navarre-Sitchler, A. (2023). Fracture intensity impacts on reaction front propagation and mineral weathering in three-dimensional fractured media. *Water Resources Research*, *59*(2), e2022WR032121. https://doi.org/10.1029/2022WR032121

Baqer, Y., & Chen, X. (2022). A review on reactive transport model and porosity evolution in the porous media. *Environmental Science and Pollution Research*, *29*(32), 47873–47901. https://doi.org/10.1007/s11356-022-20466-w

Bouzidi, M., Firdaouss, M., & Lallemand, P. (2001). Momentum transfer of a Boltzmann-lattice fluid with boundaries. *Physics of Fluids*, *13*(11), 3452–3459. https://doi.org/10.1063/1.1399290

Carslaw, H. S., & Jaeger, J. C. (1986). *Conduction of heat in solids* (2nd ed.). Oxford University Press.

Chen, L., Kang, Q., Robinson, B. A., He, Y.-L., & Tao, W.-Q. (2013). Pore-scale modeling of multiphase reactive transport with phase transitions and dissolution-precipitation processes in closed systems. *Physical Review E*, *87*(4), 043306. https://doi.org/10.1103/PhysRevE.87.043306

Chen, L., Kang, Q., Viswanathan, H. S., & Tao, W.-Q. (2014). Pore-scale study of dissolution-induced changes in hydrologic properties of rocks with binary minerals. *Water Resources Research*, *50*(12), 9343–9365. https://doi.org/10.1002/2014WR015646

Cui, J., Yang, F., Yang, T. H., & Yang, G. F. (2019). Numerical study of stainless steel pitting process based on the lattice Boltzmann method. *International Journal of Electrochemical Science*, *14*(2), 1529–1545. https://doi.org/10.20964/2019.02.47

Danner, T., Eswara, S., Schulz, V. P., & Latz, A. (2016). Characterization of gas diffusion electrodes for metal-air batteries. *Journal of Power Sources*, *324*, 646–656. https://doi.org/10.1016/j.jpowsour.2016.05.108

Danner, T., & Latz, A. (2019). On the influence of nucleation and growth of S8 and Li2S in lithium-sulfur batteries. *Electrochimica Acta*, *322*, 134719. https://doi.org/10.1016/j.electacta.2019.134719

d'Humières, D., & Ginzburg, I. (2009). Viscosity independent numerical errors for lattice Boltzmann models: From recurrence equations to "magic" collision numbers. *Computers and Mathematics with Applications*, *58*(5), 823–840. https://doi.org/10.1016/j.camwa.2009.02.008

Fang, W.-Z., Qiao, R., Kang, Q., & Tao, W.-Q. (2021). Pore-scale simulation of reactive transport processes in lithium-oxygen batteries. *International Communications in Heat and Mass Transfer*, *129*, 105740. https://doi.org/10.1016/j.icheatmasstransfer.2021.105740

Ginzburg, I., Verhaeghe, F., & D'Humières, D. (2008). Study of simple hydrodynamic solutions with the two-relaxation-times lattice Boltzmann scheme. *Communications in Computational Physics*, *3*(3), 519–581.

Guiltinan, E. J., Santos, J. E., Cardenas, M. B., Espinoza, D. N., & Kang, Q. (2021). Two-phase fluid flow properties of rough fractures with heterogeneous wettability: Analysis with lattice Boltzmann simulations. *Water Resources Research*, *57*(1), e2020WR027943. https://doi.org/10.1029/2020WR027943

He, X., Zou, Q., Luo, L.-S., & Dembo, M. (1997). Analytic solutions of simple flows and analysis of nonslip boundary conditions for the lattice Boltzmann BGK model. *Journal of Statistical Physics*, *87*(1–2), 115–136. https://doi.org/10.1007/BF02181482

Hiorth, A., Jettestuen, E., Cathles, L. M., & Madland, M. V. (2013). Precipitation, dissolution, and ion exchange processes coupled with a lattice Boltzmann advection diffusion solver. *Geochimica et Cosmochimica Acta*, *104*, 99–110. https://doi.org/10.1016/j.gca.2012.11.019

Jiang, M., Xu, Z., & Zhou, Z. (2021). Pore-scale investigation on reactive flow in porous media considering dissolution and precipitation by LBM. *Journal of Petroleum Science and Engineering*, *204*, 108712. https://doi.org/10.1016/j.petrol.2021.108712

Ju, L., Zhang, C., & Guo, Z. (2020). Local reactive boundary scheme for irregular geometries in lattice Boltzmann method. *International Journal of Heat and Mass Transfer*, *150*, 119314. https://doi.org/10.1016/j.ijheatmasstransfer.2020.119314

Jung, H., & Meile, C. (2021). Pore-scale numerical investigation of evolving porosity and permeability driven by biofilm growth. *Transport in Porous Media*, *139*(2), 203–221. https://doi.org/10.1007/s11242-021-01654-7

Kang, Q., & Lichtner, P. C. (2013). A lattice Boltzmann method for coupled fluid flow, solute transport, and chemical reaction. In M. Ehrhardt (Ed.), *Progress in computational physics volume 3: Novel trends in lattice-Boltzmann methods* (pp. 184–198). BENTHAM SCIENCE PUBLISHERS. https://doi.org/10.2174/978160805716011303001O

Kang, Q., Lichtner, P. C., & Janecky, D. R. (2010). Lattice Boltzmann method for reacting flows in porous media. *Advances in Applied Mathematics and Mechanics*, *2*(5), 545–563. https://doi.org/10.4208/aamm.10-10S02

Kang, Q., Lichtner, P. C., & Zhang, D. (2006). Lattice Boltzmann pore-scale model for multicomponent reactive transport in porous media. *Journal of Geophysical Research*, *111*(5), 1–12. https://doi.org/10.1029/2005JB003951

Kang, Q., Lichtner, P. C., & Zhang, D. (2007). An improved lattice Boltzmann model for multicomponent reactive transport in porous media at the pore scale. *Water Resources Research*, *43*(12), W12S14. https://doi.org/10.1029/2006WR005551

Kang, Q., Zhang, D., & Chen, S. (2002). Unified lattice Boltzmann method for flow in multiscale porous media. *Physical Review E - Statistical Physics, Plasmas, Fluids, and Related Interdisciplinary Topics*, *66*(5), 11. https://doi.org/10.1103/PhysRevE.66.056307

Kashani, E., Mohebbi, A., Feili Monfared, A. E., & Raoof, A. (2022). Non-linear boundary conditions for the convection-diffusion equation in lattice Boltzmann framework. *Chemical Engineering Science*, *247*, 116925. https://doi.org/10.1016/j.ces.2021.116925

Kellers, B., Lautenschlaeger, M. P., Weinmiller, J., Krumbein, L., Hein, S., Danner, T., & Latz, A. (2023). High-performance computing in battery development: From pore scale to continuum. In W. E. Nagel, D. H. Kröner, & M. M. Resch (Eds.), *HPC and data intensive computing in Baden-Württemberg. Stuttgart (HLRS) 2022*. (Accepted).

Khirevich, S., Ginzburg, I., & Tallarek, U. (2015). Coarse- and fine-grid numerical behavior of MRT/TRT lattice-Boltzmann schemes in regular and random sphere packings. *Journal of Computational Physics*, *281*, 708–742. https://doi.org/10.1016/j.jcp.2014.10.038

Krause, M. J., Kummerländer, A., Avis, S. J., Kusumaatmaja, H., Dapelo, D., Klemens, F., et al. (2021). OpenLB—Open source lattice Boltzmann code. *Computers & Mathematics with Applications*, *81*, 258–288. https://doi.org/10.1016/j.camwa.2020.04.033

Krüger, T., Kusumaatmaja, H., Kuzmin, A., Shardt, O., Silva, G., & Viggen, E. M. (2017). *The lattice Boltzmann method: Principles and practice*. Springer International Publishing. https://doi.org/10.1007/978-3-319-44649-3

Kumar, A. (2004). Isotropic finite-differences. *Journal of Computational Physics*, *201*(1), 109–118. https://doi.org/10.1016/j.jcp.2004.05.005

Latt, J., Malaspinas, O., Kontaxakis, D., Parmigiani, A., Lagrava, D., Brogi, F., et al. (2021). Palabos: Parallel lattice Boltzmann solver. *Computers & Mathematics with Applications*, *81*, 334–350. https://doi.org/10.1016/j.camwa.2020.03.022

Lautenschlaeger, M. P., Prifling, B., Kellers, B., Weinmiller, J., Danner, T., Schmidt, V., & Latz, A. (2022). Understanding electrolyte filling of lithium-ion battery electrodes on the pore scale using the lattice Boltzmann method. *Batteries & Supercaps*, *5*(7). https://doi.org/10.1002/batt.202200090

Lautenschlaeger, M. P., Weinmiller, J., Kellers, B., Danner, T., & Latz, A. (2022). Homogenized lattice Boltzmann model for simulating multi-phase flows in heterogeneous porous media. *Advances in Water Resources*, *170*, 104320. https://doi.org/10.1016/j.advwatres.2022.104320

Lautenschlaeger, M. P., Weinmiller, J., Kellers, B., Jahnke, T., Danner, T., & Arnulf, L. (2023). Lattice Boltzmann simulation of flow, transport and reactions in battery components. In W. E. Nagel, D. H. Kröner, & M. M. Resch (Eds.), *High performance computing in science and engineering '22. Stuttgart (HLRS) 2022*. Springer Cham. (Accepted).

Lei, T., & Luo, K. H. (2022). *Pore-scale study of coke formation and combustion in porous media using lattice Boltzmann method*. Proceedings of the Combustion Institute. https://doi.org/10.1016/j.proci.2022.09.053

Li, H., Yang, W., Huang, H., Chevalier, S., Sassi, M., Zhang, T., et al. (2015). Pore-scale lattice Boltzmann simulation of oil-water flow in carbonate rock with variable wettability. In *Day 4 Thu, November 12, 2015*. D041S070R006. SPE. https://doi.org/10.2118/177548-MS

Li, L., Mei, R., & Klausner, J. F. (2017). Lattice Boltzmann models for the convection-diffusion equation: D2Q5 vs D2Q9. *International Journal of Heat and Mass Transfer*, *108*, 41–62. https://doi.org/10.1016/j.ijheatmasstransfer.2016.11.092

Liu, H., Sun, S., Wu, R., Wei, B., & Hou, J. (2021). Pore-scale modeling of spontaneous imbibition in porous media using the lattice Boltzmann method. *Water Resources Research*, *57*(6), e2020WR029219. https://doi.org/10.1029/2020WR029219

Looije, N., Gillissen, J., Sundaresan, S., & Van den Akker, H. (2018). Introducing a variable speed of sound in single-component lattice Boltzmann simulations of isothermal fluid flows. *Computers & Fluids*, *167*, 129–145. https://doi.org/10.1016/j.compfluid.2018.02.037

Meng, X., & Guo, Z. (2016). Boundary scheme for linear heterogeneous surface reactions in the lattice Boltzmann method. *Physical Review E*, *94*(5), 053307. https://doi.org/10.1103/PhysRevE.94.053307

Molins, S., Soulaine, C., Prasianakis, N. I., Abbasi, A., Poncet, P., Ladd, A. J. C., et al. (2020). *Simulation of mineral dissolution at the pore scale with evolving fluid-solid interfaces: Review of approaches and benchmark problem set*. Computational Geosciences. https://doi.org/10.1007/s10596-019-09903-x

Patel, R. A. (2016). *Lattice Boltzmann method based framework for simulating physico-chemical processes in heterogeneous porous media and its application to cement paste (Unpublished doctoral dissertation)*. Ghent University.

Patel, R. A., Churakov, S. V., & Prasianakis, N. I. (2021). A multi-level pore scale reactive transport model for the investigation of combined leaching and carbonation of cement paste. *Cement and Concrete Composites*, *115*, 103831. https://doi.org/10.1016/j.cemconcomp.2020.103831

Patel, R. A., Perko, J., Jacques, D., De Schutter, G., Van Breugel, K., & Ye, G. (2014). A versatile pore-scale multicomponent reactive transport approach based on lattice Boltzmann method: Application to portlandite dissolution. *Physics and Chemistry of the Earth*, *70–71*, 127–137. https://doi.org/10.1016/j.pce.2014.03.001

Pedersen, J., Jettestuen, E., Vinningland, J. L., & Hiorth, A. (2014). Improved lattice Boltzmann models for precipitation and dissolution. *Transport in Porous Media*, *104*(3), 593–605. https://doi.org/10.1007/s11242-014-0353-0

Pereira, G. G. (2022). Numerical modelling of reactive flows through porous media. *Geosciences*, *12*(4), 153. https://doi.org/10.3390/geosciences12040153

Přikryl, J., Jha, D., Stefánsson, A., & Stipp, S. (2017). Mineral dissolution in porous media: An experimental and modeling study on kinetics, porosity and surface area evolution. *Applied Geochemistry*, *87*, 57–70. https://doi.org/10.1016/j.apgeochem.2017.05.004

Ren, J., Guo, P., Guo, Z., & Wang, Z. (2015). A lattice Boltzmann model for simulating gas flow in Kerogen Pores. *Transport in Porous Media*, *106*(2), 285–301. https://doi.org/10.1007/s11242-014-0401-9

Sarkezi-Selsky, P., Schmies, H., Kube, A., Latz, A., & Jahnke, T. (2022). Lattice Boltzmann simulation of liquid water transport in gas diffusion layers of proton exchange membrane fuel cells: Parametric studies on capillary hysteresis. *Journal of Power Sources*, *535*, 231381. https://doi.org/10.1016/j.jpowsour.2022.231381

Soulaine, C., Roman, S., Kovscek, A., & Tchelepi, H. A. (2017). Mineral dissolution and wormholing from a pore-scale perspective. *Journal of Fluid Mechanics*, *827*, 457–483. https://doi.org/10.1017/jfm.2017.499

Sullivan, S., Johns, M., Matthews, S., & Fisher, A. (2005). Lattice Boltzmann simulations of electrolysis reactions: Microfluidic voltammetry. *Electrochemistry Communications*, *7*(12), 1323–1328. https://doi.org/10.1016/j.elecom.2005.09.001

Sullivan, S., Sani, F., Johns, M., & Gladden, L. (2005). Simulation of packed bed reactors using lattice Boltzmann methods. *Chemical Engineering Science*, *60*(12), 3405–3418. https://doi.org/10.1016/j.ces.2005.01.038

Tian, Z., & Wang, J. (2017). Lattice Boltzmann simulation of $CO_2$ reactive transport in network fractured media: LBM $CO_2$ reactive transport. *Water Resources Research*, *53*(8), 7366–7381. https://doi.org/10.1002/2017WR021063

Verhaeghe, F., Arnout, S., Blanpain, B., & Wollants, P. (2006). Lattice-Boltzmann modeling of dissolution phenomena. *Physical Review E - Statistical, Nonlinear and Soft Matter Physics*, *73*(3), 1–10. https://doi.org/10.1103/PhysRevE.73.036316

Walsh, S. D. C., & Saar, M. O. (2010). Interpolated lattice Boltzmann boundary conditions for surface reaction kinetics. *Physical Review E*, *82*(6), 066703. https://doi.org/10.1103/PhysRevE.82.066703

Wang, M., & Zhu, W. (2018). Pore-scale study of heterogeneous chemical reaction for ablation of carbon fibers using the lattice Boltzmann method. *International Journal of Heat and Mass Transfer*, *126*, 1222–1239. https://doi.org/10.1016/j.ijheatmasstransfer.2018.05.133

Xie, X., Zhao, W., & Lin, P. (2021). A simple and efficient curved boundary scheme of the lattice Boltzmann method for Robin boundary conditions of convection–diffusion equations. *Applied Mathematics Letters*, *122*, 107536. https://doi.org/10.1016/j.aml.2021.107536

Xu, A., Zhao, T. S., Shi, L., & Xu, J. B. (2018). Lattice Boltzmann simulation of mass transfer coefficients for chemically reactive flows in porous media. *Journal of Heat Transfer*, *140*(5), 052601. https://doi.org/10.1115/1.4038555

Zhang, C., Kaito, K., Hu, Y., Patmonoaji, A., Matsushita, S., & Suekane, T. (2021). Influence of stagnant zones on solute transport in heterogeneous porous media at the pore scale. *Physics of Fluids*, *33*(3), 036605. https://doi.org/10.1063/5.0038133

Zhang, D., Li, S., & Li, Y. (2021). Pore-scale investigation on the effect of gas-liquid phase separation on reactive flow in a horizontal rough fracture using the lattice Boltzmann method. *Chemical Engineering Science*, *236*, 116483. https://doi.org/10.1016/j.ces.2021.116483

Zhang, L., Zhang, C., Zhang, K., Zhang, L., Yao, J., Sun, H., & Yang, Y. (2019). Pore-scale investigation of methane hydrate dissociation using the lattice Boltzmann method. *Water Resources Research*, *55*(11), 8422–8444. https://doi.org/10.1029/2019WR025195

Zhang, T., Shi, B., Guo, Z., Chai, Z., & Lu, J. (2012). General bounce-back scheme for concentration boundary condition in the lattice-Boltzmann method. *Physical Review E*, *85*(1), 016701. https://doi.org/10.1103/PhysRevE.85.016701